Bone 123 (2019) 8–17

Contents lists available at ScienceDirect

Bone

journal homepage: www.elsevier.com/locate/bone

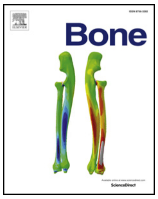

Full Length Article

Ultrashort echo time magnetic resonance imaging (UTE-MRI) of cortical bone correlates well with histomorphometric assessment of bone microstructure

Saeed Jerban[a,*], Yajun Ma[a], Jonathan H. Wong[b], Amin Nazaran[a], Adam Searleman[a], Lidi Wan[a], Judith Williams[b], Jiang Du[a], Eric Y. Chang[b,a,**]

[a] Department of Radiology, University of California, San Diego, CA, USA
[b] Radiology Service, VA San Diego Healthcare System, San Diego, CA, USA

ARTICLE INFO

Keywords:
Cortical bone
Ultrashort echo time
Porosity
Micropores
Histology
Micro computed tomography

ABSTRACT

Ultrashort echo time magnetic resonance imaging (UTE-MRI) techniques have been increasingly used to assess cortical bone microstructure. High resolution micro computed tomography (µCT) is routinely employed for validating the MRI-based assessments. However, water protons in cortical bone may reside in micropores smaller than the detectable size ranges by µCT. The goal of this study was to evaluate the upper limit of UTE-MRI and compare its efficacy to µCT at determining bone porosity ex vivo. This study investigated the correlations between UTE-MRI based quantifications and histomorphometric measures of bone porosity that cover all pores larger than 1 µm. Anterior tibial midshaft specimens from eleven donors (51 ± 16 years old, 6 males, 5 females) were scanned on a clinical 3 T-MRI using UTE magnetization transfer (UTE-MT, three power levels and five frequency offsets) and UTE-T2* sequences. Two-pool MT modeling and bi-component exponential T2* fitting were performed on the MRI datasets. Specimens were then scanned by µCT at 9 µm voxel size. Histomorphometry was performed on hematoxylin and eosin (H&E) stained slides imaged at submicron resolution. Macromolecular fraction from MT modeling, bi-component T2* fractions, and short component T2* showed strong correlations ($R > 0.7$, $p < 0.01$) with histomorphometric total and large-pores ($> 40\,\mu m$) porosities as well as with µCT-based porosity. UTE-MRI could also assess small pores variations with moderate correlations ($R > 0.5$, $p < 0.01$). The UTE-MRI techniques can detect variations of bone porosity comprised of pores below the range detectable by µCT. Such fine pore variations can contribute differently to the development of bone diseases or to the bone remodeling process, however, this needs to be investigated. In scanned specimens, major porosity changes were from large pores, therefore the µCT employment was likely adequate to validate UTE-MRI biomarkers.

1. Introduction

Cortical bone comprises approximately 80% of human bone mass and plays a major role in load bearing [1,2]. Porosity in cortical bone can determine bone mechanical properties and its fracture risk [3,4]. Employing magnetic resonance imaging (MRI) for cortical bone assessment has become of great interest due to the relatively safe nature of MRI compared to methods which use ionizing radiation such as computed tomography (CT) [5–7]. Although clinical MRI shows void signal for cortical bone, ultrashort echo time (UTE) MRI can image and quantitatively assess cortical bone [5–14]. More specifically, UTE-MRI can acquire signal several microseconds (8–32 microseconds depending on the read out trajectory) after radiofrequency (RF) excitation (8–60 microseconds depending on the flip angle) before the rapid transverse magnetization decay of cortical bone [1,2].

Water in bone exists in two main forms: first, bound to the collagen

---

Abbreviations: MR, magnetic resonance; MRI, magnetic resonance imaging; 3D, three-dimensional; 3D- UTE, three-dimensional ultrashort echo time imaging; RF, radio frequency; FOV, field of view; MT, magnetization transfer; ROI, region of interest; TE, echo time; TR, repetition time; CT, computed tomography; µCT, micro computed tomography; MMF, macromolecules fraction; $T2_{MM}$, macromolecular T2; FA, flip angle; BMD, bone mineral density; PBS, phosphate buffered saline; H&E, hematoxylin and eosin

* Correspondence to: S. Jerban, Department of Radiology, University of California, 9500 Gilman Dr., San Diego, CA 92093, USA.

** Correspondence to: E. Y. Chang, Radiology Service, VA San Diego Healthcare System, San Diego, CA 92161, USA.

E-mail addresses: sjerban@ucsd.edu (S. Jerban), e8chang@ucsd.edu (E.Y. Chang).

https://doi.org/10.1016/j.bone.2019.03.013
Received 24 December 2018; Received in revised form 8 March 2019; Accepted 11 March 2019

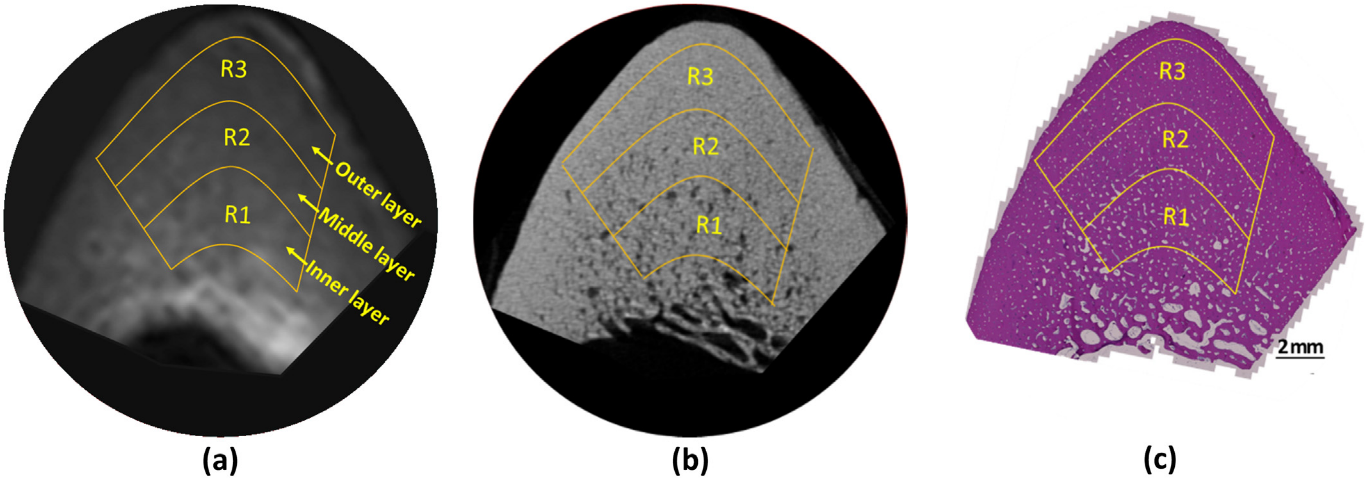

Fig. 1. Selected ROIs at three different bone layers on a representative bone specimen (Male, 71 years old) illustrated on (a) UTE-MRI (250 μm pixel size), (b) μCT (9 μm pixel size), and (c) histology (H&E stained, 0.2 μm pixel size) images.

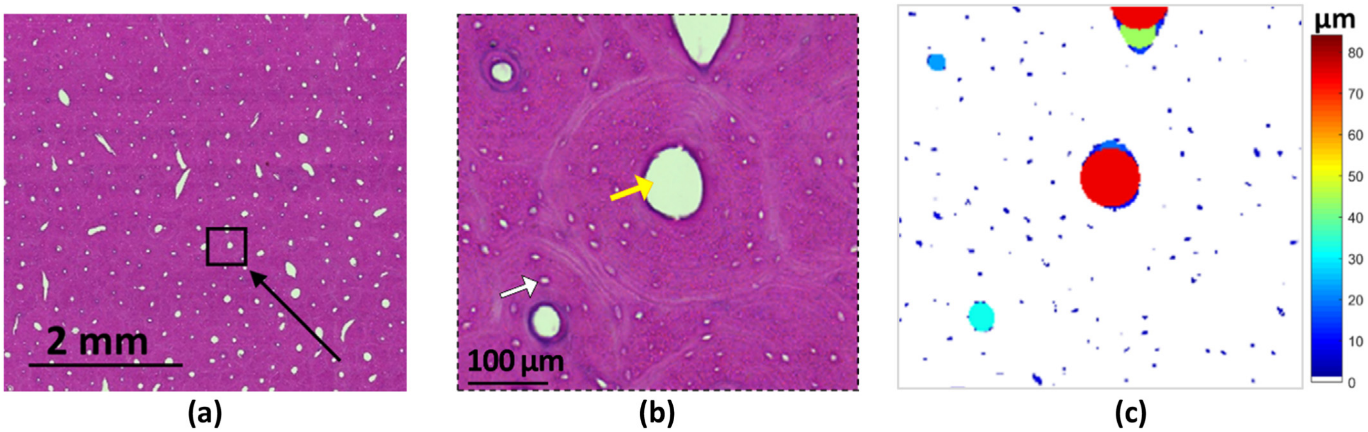

Fig. 2. (a) a 5 × 5 mm cropped histological H&E stained image of cortical bone specimen with many visible Haversian canals (white spots). (b) Enlarged histological image within the selected black box in Fig. 2a. Haversian canals and lacunae are indicated with yellow and white arrows, respectively. (c) Pore size pixel map of the selected region in the histology section. Pore size at each pixel is defined as the diameter of the largest covering circle.

matrix (bound water) and second, as free water in bone pores (pore water) [1,2]. Bound water can be considered an indirect measure of the collagen matrix, while pore water represents the bone porosity, and both can affect the mechanical properties of cortical bone [3,10,11,15]. Different quantitative UTE-MRI techniques have been reported to distinguish between bound and pore water, employing their significantly different MRI properties [1,2,5–10,16–19]. Bi-component exponential fitting of T2* signal decay has been used to distinguish and evaluate the pore water and bound water fractions in bone [2,16]. Bi-component fitting also provides the average T2* values of both pore and bound water pools. Bi-component fitting results have shown good correlations with intracortical bone porosity measured with high resolution micro computed tomography (μCT) [16]. Other UTE-MRI techniques such as dual-echo UTE imaging (i.e., porosity index) [8], direct pore water imaging after nulling bound water [10], and tri-component T2* analysis by modeling fat signal [17] have also been reported to evaluate pore water content in cortical bone, which demonstrated good correlations with bone porosity, as validated with μCT.

In an alternative approach, modeling the magnetization transfer (MT) from macromolecules to water enabled measuring of the macromolecular protons fraction (MMF) [20,21]. With MT techniques, an RF pulse with a defined frequency offset from the water protons' resonance frequency is used to saturate macromolecular protons. The magnitude of the transferred saturation to water protons correlates with MMF in the tissue. MMF from two-pool 3D-UTE-MT modeling and MT ratio have demonstrated significant correlations with human bone porosity, as measured with μCT [22,23]. Significant MMF variation has been observed in cortical bone after bone stress injury, likely due to induction of microcracks [24].

Intracortical bone porosity includes a range of pore classes and sizes, including Haversian canals (10–200 μm), lacunae (1–10 μm), and canaliculi (0.1–1 μm) [25,26]. The sufficiency of employing μCT for validating the porosity estimated by UTE-MRI [8,10,16,22,23] is questionable, as μCT can only measure a portion of large Haversian canals. A voxel size of 9 μm has been used in several studies, as this is the lowest voxel size available in most current μCT scanners. Such resolution is practically adequate to accurately characterize pores larger than 40 μm in size (4 voxels approx.). Pores smaller than 4 voxels may be removed during the denoising steps in image processing and the remaining small pores will be highly underestimated in size measurement [27,28]. However, the UTE-MRI signal presumably involves all water protons, even those residing in micropores below the μCT detectable range (i.e., lacunae and canaliculi). The reliability of using high resolution μCT for validating the UTE-MRI based measures of cortical bone has not been well investigated. Additionally, the correlations between UTE-MRI quantifications of cortical bone and small pores of bone are yet to be understood.

The goal of this study was to evaluate the upper limit of UTE MRI and compare its efficacy to μCT at determining bone porosity ex vivo. Specifically, this study was aimed to determine the correlations of two

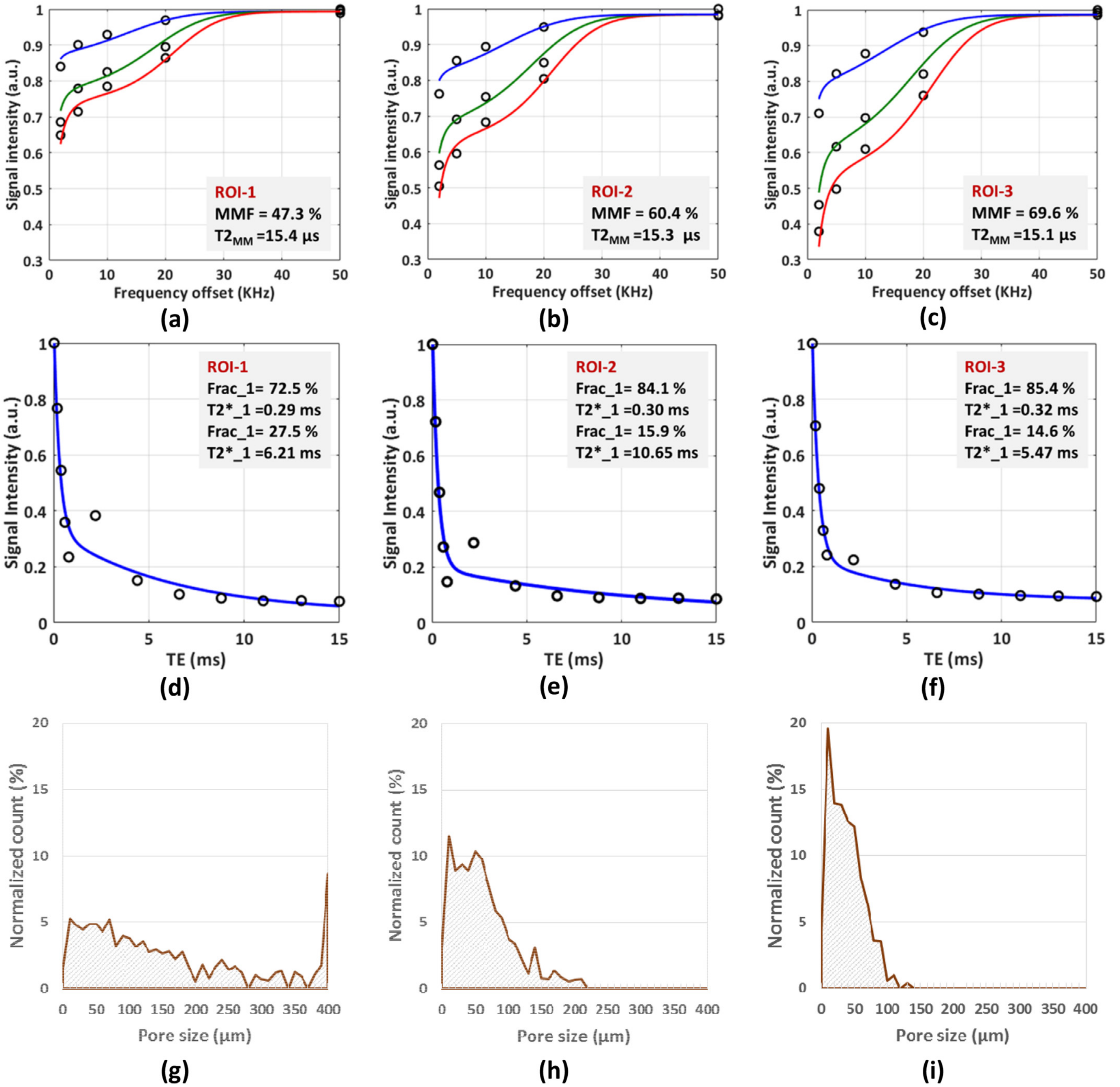

Fig. 3. MRI-based and histomorphometric analyses for three exemplary ROIs at three different cortical bone layers (Fig. 1). (a–c) The two-pool MT modeling analyses in (a) ROI-1, (b) ROI-2, and (c) ROI-3 using three pulse saturation powers (500° in blue, 750° in green, and 1000° in red) and five frequency offsets (5, 10, 20, 50 kHz). MMF and $T2_{MM}$ refer to macromolecular fraction and macromolecular T2, respectively. (d–f) Bi-component exponential fitting of the T2* decay within (d) ROI-1, (e) ROI-2, and (f) ROI-3. The oscillating actual data points indicates the presence of fat particularly in ROI-1 and ROI-2 near the endosteum. (g–i) Pore size distribution obtained from histomorphometric analyses within (g) ROI-1, (h) ROI-2, and (i) ROI-3. Histomorphometric porosity and pore size for ROI-1 to -3 were 33.1, 13.9, and 7.1% and 221, 83, 49 µm, respectively. The µCT-based porosity was 21.2, 8.2, and 1.7% for ROI-1 to -3, respectively. (For interpretation of the references to color in this figure legend, the reader is referred to the web version of this article.)

common UTE-MRI based techniques with intracortical bone porosities, as measured with histomorphometric methods and with µCT. In addition to the µCT scans at 9 µm voxel size, the microscopic images of histology slides (0.2 µm pixel size) provide access to all Haversian canals and almost all lacunae pores. This study complements the previous evaluations of UTE-MRI techniques validated with µCT [16,22] through clarifying the UTE-MRI capability for assessing all intracortical bone porosities larger than 1 µm. The two UTE-MRI methods considered for this study were two-pool MT modeling and bi-component T2* fitting, techniques which have been the recent focus of this research group [16,22].

2. Materials and methods

2.1. Sample preparation

Cortical bone specimens were harvested from eleven fresh-frozen tibial midshafts of relatively young donors (51 ± 16 years old, 5

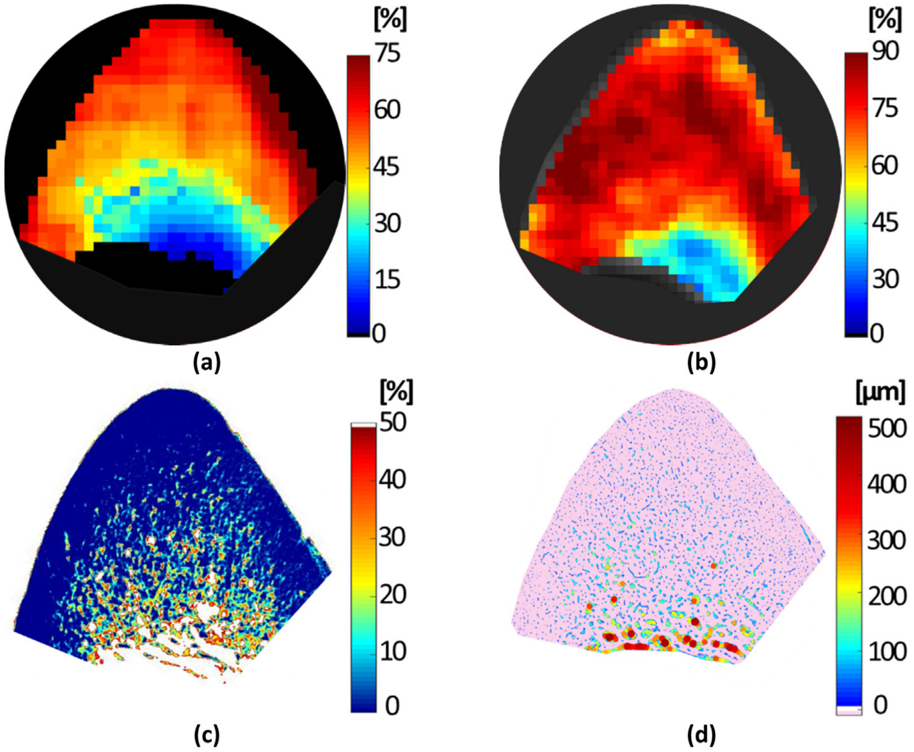

Fig. 4. (a) Macromolecular fraction (MMF) from MT modeling, (b) Frac1 (short-T2* component) from bi-component T2* fitting, (c) μCT-based porosity, and (d) histomorphometry-based pore size maps of a representative anterior tibial bone specimen (71-year-old male).

females and 6 males), provided by a nonprofit whole-body donation company (United Tissue Network, Phoenix, AZ). Tibial midshafts were cut to 25 mm in length using a commercial band saw. After removal of the bone marrow, the anterior portions of the tibias were excised using a low-speed diamond saw (Isomet 1000, Buehler, IL, USA) in order to fit the bone specimen in a homemade 1-inch diameter solenoid coil and to avoid complications in histology study caused by large specimens. The final dimension of the specimens was approximately 20 × 20 × 25 mm.

2.2. UTE-MR imaging

All bone specimens were immersed in phosphate-buffered saline (PBS) for 2 h at room temperature before the MRI scans. Each sample was placed in a 30-mL syringe filled with perfluoropolyether (Fomblin, Ausimont, Thorofare, NJ) to minimize dehydration and susceptibility artifacts. The UTE-MRI scans were performed on a 3T clinical scanner (Signa HDx, GE Healthcare Technologies, Milwaukee, WI) using a homemade 1-inch diameter solenoid transmit/receive coil. The UTE scans involved the three following quantitative protocols: A) six sets of dual-echo 3D-UTE-Cones sequences (TR = 24.3 ms, TEs = 0.032, 0.2, 0.4, 0.6, 0.8, 2.2, 4.4, 6.6, 8.8, 11, 13, 15 ms, with a total scan time of 14 min) for T2*measurements, B) a variable TR 3D-UTE-Cones sequence (TE = 0.032 ms, TRs = 5.9, 10, 20, 40, 60, and 100 ms, flip angle (FA) = 20°, rectangular RF pulse with a duration of 30 μs, with a total scan time of 16 min) for T1 measurement, which is a prerequisite for MT modeling, and C) a set of 3D-UTE-Cones-MT sequences (MT saturation pulse power = 500°, 750°, and 1000°; frequency offset = 2, 5, 10, 20, and 50 kHz; FA = 10°, with a total scan time of 15 min) for two-pool MT modeling [20,21,29]. Other imaging parameters included: field of view (FOV) = 40 mm, matrix = 160 × 160, slice thickness = 3 mm, receiver bandwidth = 62.5 kHz, and total scan time = 45 min. Features of the 3D-UTE-Cones sequence have been described in previous studies [30–32]. The 3D-UTE-Cones sequence employs a short rectangular pulse excitation followed by a 3D Cones trajectory. The 3D k-space is divided into multiple cones, with twisted radial trajectories along each cone. The Cones sequence is more time-efficient than radial trajectories in covering 3D k-space. The 3D-UTE-Cones sequence resolves the limitations associated with 2D-UTE sequences, which are very sensitive to eddy currents because of their half-pulse excitation. The two-pool UTE-MT modeling was previously described in detail by Ma et al. [20,21,29].

2.3. Micro-computed tomography (μCT)

Bone specimens were scanned using a Skyscan 1076 (Kontich, Belgium) μCT scanner at 9 μm isotropic voxel size. For measuring BMD in addition to bone porosity, specimens were scanned in the presence of two hydroxyapatite phantoms (0.25 and 0.5 g/cm^3). Other scanning parameters were as follows: a 0.05 mm aluminum plus a 0.038 mm copper filter, 100 kV, 100 mA, 0.4° rotation step, and 5 frame-averaging.

2.4. Histology and histomorphometry

To measure the intracortical bone porosity through histomorphometric analyses, a 2-mm thick slice was cut from the middle of each scanned specimen using a low-speed diamond saw (Isomet 1000, Buehler, IL, USA). These eleven bone slices were fixed in zinc-formalin fixative (Anatech, Battle Creek MI, USA) for five days at room temperature. The fixed slices were decalcified via several changes of 10% formic acid over two weeks at room temperature. Decalcified slices were soaked in 30% sucrose in PBS, then frozen for immediate cryo-sectioning at 6 μm thickness. Finally, the thin decalcified sections were collected onto slides and stained by hematoxylin and eosin (H&E). One representative histology section was selected per bone specimen and imaged using a virtual microscopy scanner (Axio Scan.Z1, Carl Zeiss, Jena, Germany) for porosity and pore size calculations.

Table 1

Mean, standard deviation and range of the UTE-MRI, μCT, and histomorphometric measures in the selected ROIs.

Bi-component T2* fitting			MT-modeling		μCT		Histomorphometry Porosity (%)			Histomorphometry Pore size (μm)		
Frac1 (%)	T2*1 (ms)	T2*2 (ms)	MMF (%)	T_{2MM} (μs)	Porosity (%)	BMD (gr/cm3)	All	Small pores	Large pores	All	Small pores	Large pores
75.8 ± 9.0 [52–89]	0.33 ± 0.05 [0.25–0.42]	6.0 ± 1.8 [3.4–10.6]	55.1 ± 14.7 [25.5–77.4]	14.8 ± 0.7 [13.2–16.0]	15 ± 10 [1–38]	1.05 ± 0.11 [0.85–1.22]	14.9 ± 9.8 [3.6–40.7]	2.9 ± 1.0 [1.2–5.1]	12.0 ± 9.3 [1.2–36.8]	102 ± 56 [32–256]	19 ± 1 [16–21]	124 ± 57 [55–282]

2.5. Data analysis

UTE-MRI quantifications in one slice (3 mm thick) at the middle of the specimens were compared with histomorphometric and μCT measures. MRI, histomorphometric, and μCT comparisons were performed within three regions of interest (ROIs) defined at three different bone layers from the endosteum towards the periosteum (Fig. 1). Such ROI selection provided adequate microstructural variation to examine the UTE-MRI techniques. Finally, Pearson's correlations were calculated between UTE-MRI, histomorphometric, and μCT measures. These ROIs were considered all together in order to examine the UTE-MRI method's capability to detect the variation of bone microstructure regardless of the intracortical bone location. Based on the literature [22], the selected layers of the cortical bone possess significantly different microstructures. While this does introduce some interdependency between data points, significance levels for all correlations were assessed using non-parametric bootstrap (with resampling by specimen) to adjust for within-specimen dependence. All the data analyses were performed in MATLAB (version 2017, The Mathworks Inc., Natick, MA, USA). Statistical analyses were performed using a statistical programming language (R, version 3.2.5, R Development Core Team, Vienna, Austria).

2.5.1. Quantitative UTE-MRI analyses

Quantitative MR analyses included bi-component T2*, single-component T1, and two-pool MT modeling. For bi-component T2* fitting, a short T2* component ($T2^*_1$) and a long T2* component ($T2^*_2$) representing bound water and pore water, respectively, were assumed [2,14,33]. The signal in bi-component fitting was modeled using the following equation, $S(TE) \propto \mathrm{Frac1} \times \mathrm{Exp}\ (-\mathrm{TE}/\mathrm{T2_1}^*) + \mathrm{Frac2} \times \mathrm{Exp}\ (-\mathrm{TE}/\mathrm{T2_2}^*) + \mathrm{constant}$, where S(TE) is the normalized UTE-MRI signal, and Frac1 and Frac2 are proton fractions of short and long T2* components, respectively.

T1 measurement was performed using the following single-component fitting model, $S(TR) \propto \left(1 - \exp\left(-\frac{TR}{T1}\right)\right) + constant$, where S(TR) is the normalized UTE-MRI signal [1,2,19].

The UTE-MT analysis was accomplished by using a two-pool model to estimate MMF and macromolecular T2 ($T2_{MM}$) based on a modified rectangular pulse approximation approach [20,21,29]. In the two-pool model, the first pool is macromolecular proton pool which has a very broad spectrum or extremely short T2 (~10 μs), while the second pool is water proton pool which includes both bound and pore water protons. If the macromolecular proton magnetization is partially saturated, the acquired water signal intensity decreases due to the magnetization transfer. Details of the two-pool MT modeling are described earlier [20,21,29].

2.5.2. μCT analyses

A single gray level threshold was used for μCT image segmentation to distinguish between bone and pores. The gray level threshold was selected for each set of μCT data by investigating the gray level histograms and pore interfaces in raw images. Thresholding resulted in a stack of binary images. A porosity pixel map was generated for each bone specimen by superimposing the 333 binary images to cover the corresponding 3-mm MRI slice. BMD was calculated for each voxel using a linear function of voxel's gray level which is determined based on gray levels of hydroxyapatite phantoms. Affine image registration was used to propagate ROIs selected on MRI images onto the μCT data. Image registration was performed manually by an image processing expert in MATLAB via selecting four identical points in images from different modes (MRI, μCT, and histology).

2.5.3. Histomorphometric analyses

For histomorphometric analyses, a color-based image segmentation approach was used to distinguish between pores and bone matrix pixels in histology images. A set of morphological operations were used to

Table 2

Pearson's correlations, 95% intervals, and p values between microstructural measures (histomorphometric and μCT-based) and UTE-MRI parameters (bi-component T2* fitting and MT modeling). Significance for all correlations were assessed using non-parametric bootstrap (with resampling by specimen) to adjust for within-specimen dependence.

			Bi-component T2* fitting			MT-modeling	
			Frac1	$T2^*_1$	$T2^*_2$	MMF	$T2_{MM}$
μCT		Porosity	−0.71 [−0.89, −0.18] $p < 0.01$	−0.76 [−0.89, −0.51] $p < 0.01$	0.09 [−0.31,0.42] $p = 0.74$	−0.87 [−0.92, −0.77] $p < 0.01$	0.37 [−0.24,0.61] $p = 0.18$
		BMD	0.68 [0.17,0.83] $p < 0.01$	0.61 [0.45,0.75] $p < 0.01$	−0.06 [−0.29,0.31] $p = 0.86$	0.85 [0.70,0.91] $p < 0.01$	−0.25 [−0.68,0.43] $p = 0.50$
Histomorphometry	Porosity	All pores	−0.71 [−0.85, −0.45] $p < 0.01$	−0.71 [−0.83, −0.53] $p < 0.01$	0.11 [−0.31,0.44] $p = 0.63$	−0.81 [−0.89, −0.65] $p < 0.01$	0.61 [0.25,0.78] $p < 0.01$
		Small pores ($< 40\,\mu m$)	−0.52 [−0.74, −0.23] $p < 0.01$	−0.42 [−0.81, −0.09] $p = 0.02$	0.02 [−0.26,0.39] $p = 0.88$	−0.56 [−0.77, −0.34] $p < 0.01$	0.26 [−0.22,0.76] $p = 0.26$
		Large pores ($> 40\,\mu m$)	−0.69 [−0.83, −0.43] $p < 0.01$	−0.70 [−0.82, −0.53] $p < 0.01$	0.11 [−0.31,0.45] $p = 0.62$	−0.78 [−0.88, −0.64] $p < 0.01$	0.61 [0.29,0.78] $p < 0.01$
	Pore size	All pores	−0.55 [−0.74, −0.22] $p < 0.01$	−0.71 [−0.85, −0.53] $p < 0.01$	0.15 [−0.39,0.54] $p = 0.58$	−0.73 [−0.85, −0.55] $p < 0.01$	0.65 [0.41,0.81] $p < 0.01$
		Small pores ($< 40\,\mu m$)	−0.60 [−0.80, −0.35] $p < 0.01$	−0.42 [−0.78,0.16] $p = 0.17$	−0.19 [−0.61,0.20] $p = 0.37$	−0.51 [−0.79, −0.21] $p < 0.01$	0.27 [−0.16,0.67] $p = 0.23$
		Large pores ($> 40\,\mu m$)	−0.55 [−0.76, −0.21] $p < 0.01$	−0.70 [−0.86,0.52] $p < 0.01$	0.14 [−0.40,0.52] $p = 0.61$	−0.74 [−0.86, −0.54] $p < 0.01$	0.64 [0.39,0.80] $p < 0.01$

exclude artifacts and stain contaminations after image segmentation. Pore size at each pixel was defined as the diameter of the largest covering circle, an oft-used definition in the literature [34–36]. A pore size threshold equal to 40 μm was used for discriminating small pores from large pores that are accurately measurable with μCT. Average porosities and pore sizes within each ROI were calculated for the following three pore classes: 1) all pores, 2) small pores ($< 40\,\mu m$), and large pores ($\geq 40\,\mu m$). Affine image registration was used to propagate the ROIs selected on MRI images to histology images.

3. Results

Fig. 1 illustrates the UTE-MRI, μCT, and histology images of a representative bone specimen (71-year-old male). Three selected ROIs at three bone layers from endosteum towards periosteum are shown on the images.

Fig. 2a shows a 5×5 mm cropped histology image with several visible Haversian canals. A zoomed-in area of the selected histology section is shown in Fig. 2b with Haversian canals and lacunae arranged around the Haversian canals indicated. Pore size map of the selected region is presented in Fig. 2c, where the pore size ranges from submicron in some lacunae to a hundred micrometers in the highlighted Haversian canal at the center.

Fig. 3a–c show the two-pool MT modeling analyses within the three defined ROIs of a representative bone specimen (Fig. 1, 71-year-old male). MT modeling was performed for five off-resonance frequencies (2, 5, 10, 20, and 50 kHz) and three MT saturation pulse power levels, including 500°, 750°, and 1000°, that are indicated with blue, green, and red lines. Bi-component T2* fittings within the same three ROIs are illustrated in Fig. 3d–f. The oscillating actual data points around TE = 2 ms indicate the presence of fat in specimens, particularly in ROIs near the endosteum. Fig. 3g–i show the pore size distributions achieved through histomorphometric analyses within the same ROIs. Calculated porosities from μCT and histomorphometric analyses in ROI-1, -2, and -3 were in descending order. As expected, MMF and Frac1 in ROI-1, -2, and -3 were in ascending order. Pore size distributions shifted towards lower values for ROI-3 compared with ROI-2 and ROI-1, indicating a limited number of large pores ($> 100\,\mu m$) in the outer layer of the cortex. Histomorphometric porosity and pore size for ROI-1, -2, and -3 were 33.1, 13.9, and 7.1% and 221, 83, 49 μm, respectively. The μCT-based porosity was 21.2, 8.2, and 1.7% for ROI-1, -2, and -3, respectively.

Fig. 4a shows the generated pixel maps from MT modeling for the representative specimen shown in Fig. 1a. Frac1 pixel map from bi-component T2* fitting is shown in Fig. 4b. MMF and Frac1 pixel maps demonstrated an increasing pattern towards outer bone layer, which was more obvious in the MMF map. The μCT-based porosity pixel map for this specimen is illustrated in Fig. 4c, which is calculated by superimposing 333 μCT slices. Fig. 4d shows the pore size map obtained from histomorphometric analysis performed on a representative histology slice of the mentioned specimen. Obviously larger pores and porosity fractions were found on the endosteum side of the cortex.

The mean, standard deviation and range of the measured MRI, μCT, and histomorphometry results are presented in Table 1.

Pearson's correlations, 95% intervals, and p values between microstructural measures and UTE-MRI parameters are presented in Table 2 considering all selected ROIs. Significance for all correlations were assessed using non-parametric bootstrap (with resampling by specimen) to adjust for within-specimen dependence. Large-pore porosity ($> 40\,\mu m$) distinguished in histomorphometric analyses and the μCT-based porosity showed strong correlations with MMF, Frac1, and $T2^*_1$. MMF and Frac1 demonstrated moderate correlation with small-pores porosity ($< 40\,\mu m$). Average pore size from histomorphometric analyses demonstrated strong correlations with MMF ($R = 0.73$, $p < 0.01$) and $T2^*_1$ ($R = 0.70$, $p < 0.01$). Average size of large pores also showed strong correlations with MMF and $T2^*_1$. Average size of small pores showed poor correlations with the UTE-MRI properties. MMF also demonstrated a strong correlation with BMD ($R = 0.85$, $p < 0.01$).

Scatter plots and linear regressions of histomorphometric bone porosity and pore size (all pores, small pores and large pores) on MMF are shown in Fig. 5. As mentioned in Table 2, MMF showed higher correlations with all-pores and large-pores porosities. However, correlations with small-pores porosity were moderate. Small-pores porosity varied approximately between 1% and 5%, which was much lower than

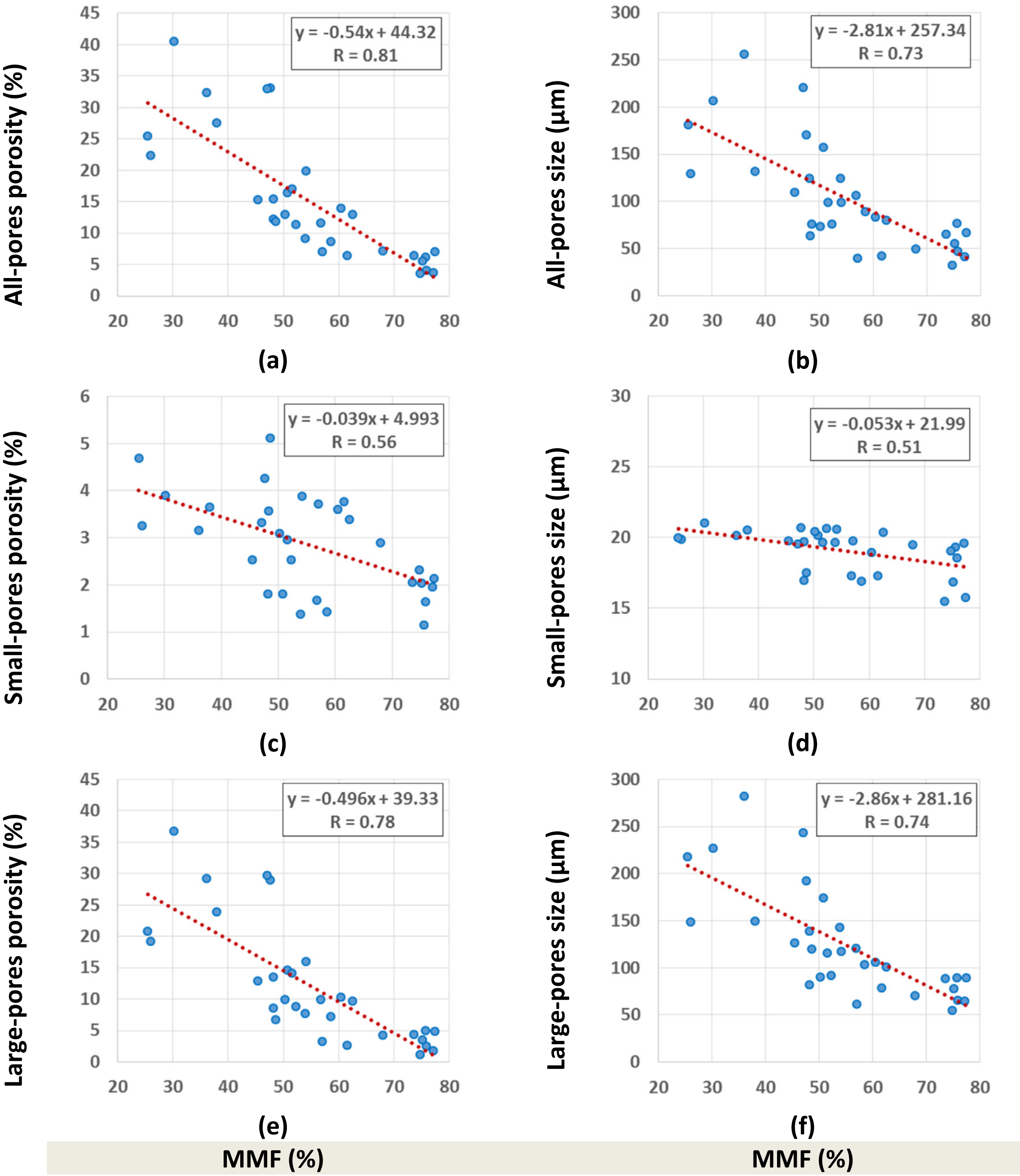

Fig. 5. Scatter plot and linear regressions of bone porosity and pore size on MMF considering (a, b) all pores, (c, d) only small pores, and (e, f) only large pores. Significance levels for these correlations were below 0.01, as measured using non-parametric bootstrap (with resampling by specimen) to adjust for within-specimen dependence.

the variation of large-pores porosity (1–35%). Average size variation of small pores was approximately between 15 µm to 22 µm.

Scatter plots and the linear regressions of histomorphometric bone porosity and pore size (all pores, small pores, and large pores) on short component fraction (Frac1) from bi-component T2* analyses are shown in Fig. 6. As mentioned in Table 1, Frac1 showed higher correlations with porosity and pore size when considering all pores or large pores. However, correlations with small-pore porosity were moderate.

Table 3 presents Pearson's correlation coefficients between µCT-based measures and histomorphometric results. The µCT-based porosity showed strong correlations with histomorphometric porosity and pore size when considering all pores or only large pores ($R > 0.70$, $p < 0.01$). Correlations were poor when considering only small pores in histomorphometric analyses ($R < 0.3$). BMD from µCT analyses showed strong correlations with average porosities from histomorphometric analyses regardless of the considered pore sizes.

4. Discussion

This study was the first to investigate the correlations between UTE-MRI biomarkers of cortical bone and histomorphometric analyses on histology images with submicron pixel size (0.2 µm). This technique enabled the study to accurately include all intracortical bone pores larger than 1 µm (all Haversian canals and lacunae) for validating the UTE-MRI techniques. This study complements the previous evaluations of UTE-MRI techniques validated with high resolution µCT-based porosity (i.e., 9 µm voxel size) [16,22]. Such µCT-based measurements would be practically accurate only for pores larger than 40 µm in size (4

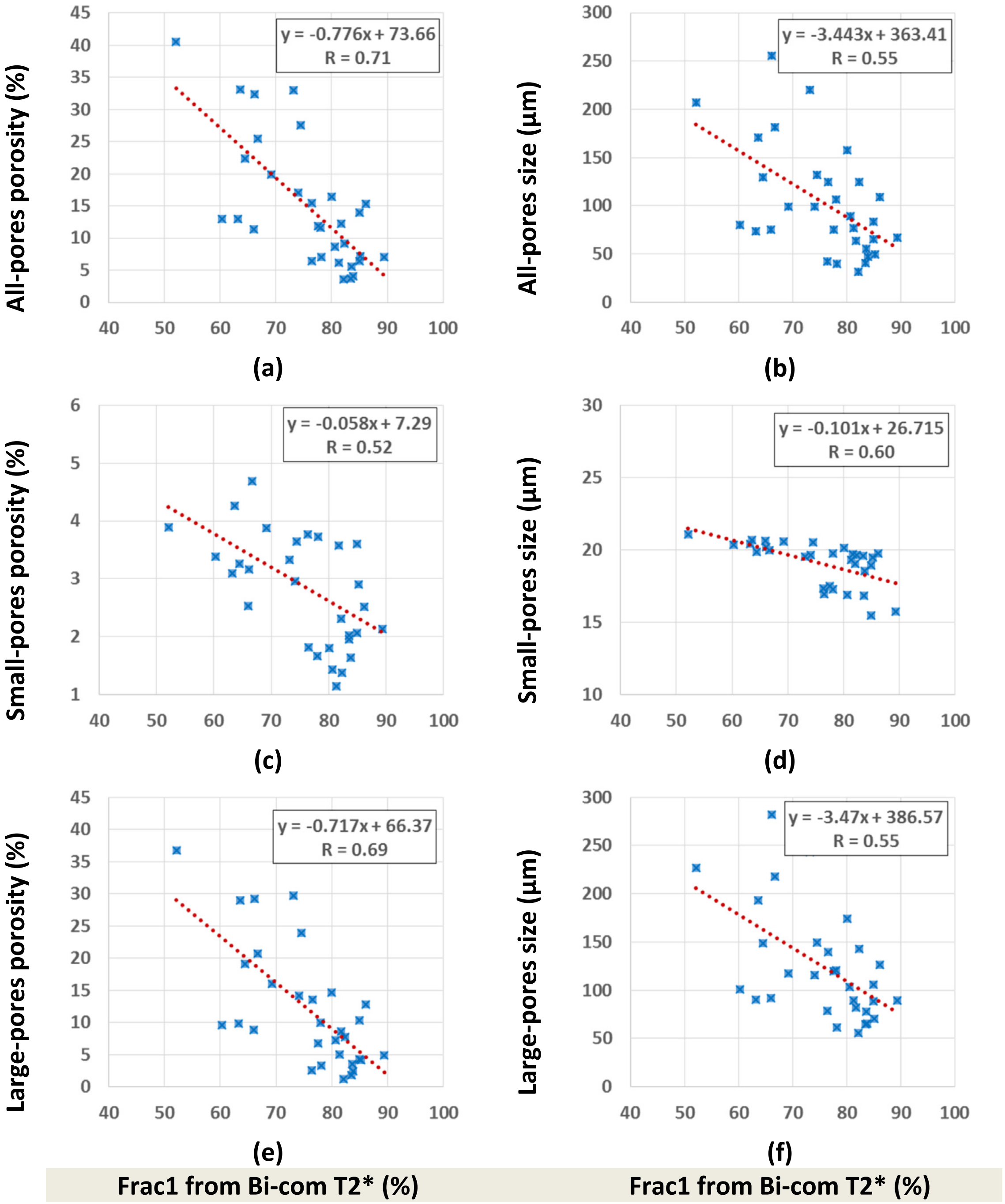

Fig. 6. Scatter plot and linear regressions of bone porosity and pore size on short component fraction (Frac1) when considering (a, b) all pores, (c, d) only small pores, and (e, f) only large pores. Significance levels for these correlations were below 0.01, as measured using non-parametric bootstrap (with resampling by specimen) to adjust for within-specimen dependence.

voxels).

The investigated UTE-MRI techniques were the two-pool MT modeling and bi-component T2* fitting, which have been the recent focus of this research group in assessing cortical bone microstructure and mechanics [1,2,16,22–24]. Bi-component T2* fitting results, as well as MMF from two-pool MT modeling, have previously shown good correlations with cortical bone porosity [16,22] and mechanics [16,24].

For the eleven studied anterior tibial bone specimens, MMF, Frac1, and $T2^*_1$ from investigated MRI properties demonstrated strong correlations with all-pores and large-pores porosities. Remarkably, these UTE-MRI properties showed moderate correlations with small porosities from histomorphometric analyses. Therefore, UTE-MRI biomarkers were capable of detecting microstructural variations in the form of large pores and small pores. Such range of variations was not detectable by high resolution μCT. This demonstrates the technique's potential for a low detectable variation of bone porosity, which in turn suggests UTE-MRI as a potentially sensitive tool to help early detection of bone diseases.

Strong correlations of MMF, Frac1, and $T2^*_1$ with porosity were valid when comparisons were performed with both histomorphometric and μCT results. Although the total porosity from histomorphometric analyses was higher than μCT-based porosity (more detectable pores in histology images), their correlations with UTE-MRI biomarkers were comparable (Table 2). The μCT-based porosity showed strong

Table 3
Pearson's correlations, 95% intervals, and p values between histomorphometric measures (porosity and pore size) and μCT-based results (porosity and BMD). Significance for all correlations were assessed using non-parametric bootstrap (with resampling by specimen) to adjust for within-specimen dependence.

			μCT	
			Porosity	BMD
Histomorphometry	Porosity	All pores	0.86 [0.74,0.95] p < 0.01	−0.81 [−0.62, −0.92] p < 0.01
		Small pores (< 40 μm)	0.29 [−0.08,0.61] p = 0.19	−0.71 [−0.83, −0.43] p < 0.01
		Large pores (> 40 μm)	0.87 [0.74,0.94] p < 0.01	−0.76 [−0.89, −0.52] p < 0.01
	Pore size	All pores	0.78 [0.61,0.90] p < 0.01	−0.65 [−0.80, −0.35] p < 0.01
		Small pores (< 40 μm)	0.26 [−0.18,0.56] p = 0.23	−0.44 [−0.72, −0.10] p = 0.06
		Large pores (> 40 μm)	0.78 [0.60,0.88] p < 0.01	−0.71 [−0.82, −0.42] p < 0.01

correlations with histomorphometric large-pores porosity (Table 3). Due to limited resolution of μCT, the porosity correlations were poor when considering only small pores in histomorphometric analyses. Interestingly, strong correlations were found between BMD and histomorphometric porosities regardless of the considered pore sizes. This indicates the BMD sensitivity to subvoxel mineral variation. The UTE-MRI and μCT correlations were consistent with the previous studies performed on different coils and different specimen dimensions [16,22].

UTE-MRI quantifications showed higher correlations with large pores compared with small pores. In other words, the variations of UTE-MRI properties in studied bone specimens could be explained better by large pore variation. This may have resulted from limited variation of small porosities in studied bone specimens which were harvested from normal donors. In the eleven studied cortical bone specimens (33 ROIs), the range of small-pores porosity (1–5%) was much lower than the range of large-pores porosity (1–35%). Consequently, μCT-based porosity measurements were likely adequate to validate the correlations between cortical bone microstructure and MRI biomarkers in studied specimens. Such correlations are most likely valid when comparisons are taking place between young, old, or osteoporotic cohorts, where large pore variation counts for the major changes in cortical bone microstructure. Nevertheless, UTE-MRI techniques enabled assessing much finer bone microstructure including all lacunae and small Haversian canals which in turn can contribute differently to bone disease development compared with large pores. Furthermore, variation of such fine micropores may be determinative factor in bone stress injuries and bone remodeling process.

MMF demonstrated higher average correlations with microstructural properties compared with bi-component T2* fitting results. This might be resulted from lower sensitivity of the two-pool MT modeling to fat presence in the cortical bone compared with bi-component T2* fitting. Bi-component T2* fitting might result to inaccurate fractions when fat is present particularly near the endosteum. Fat presence can be indicated by the oscillating actual data points in Fig. 3d–f caused by chemical shifts. Consistent correlations of MMF and Frac1 with both porosity and pore size were most likely resulted from the concurrent variations of porosity and pore size in bone specimens.

This study had several limitations. First, the studied bone specimens demonstrated limited variation of small porosities that challenged the accurate evaluation of UTE-MRI capability in small pore assessment. However, moderate correlations with small pore variations in this range (1–5%) were promising. Using synthesized biomaterials with large variation of small pores instead of bone may improve the correlation in future steps. Second, only one representative H&E histology slide was used from the middle of each bone specimen for histomorphometric analyses. Comparison of 2D histomorphometric results with those of a 3 mm-thick MRI and μCT map might introduce some errors. However, this approach was likely adequate because limited axial variation of cortical bone can be assumed at tibial midshaft for 3 mm length. Third, this study only focused on two-pool MT modeling and bi-component T2* fitting. Similar concluded patterns of correlations with small-pores and large-pores porosities are expected to be true for other UTE-MRI techniques [8,10]. However, well-designed future studies are required to achieve accurate conclusions for each specific UTE-MRI technique. Fourth, the correlation between investigated techniques and histomorphometric results were performed ex vivo and with a 1-inch homemade coil. The performance of such UTE-MRI techniques was examined before using bone specimens with a knee coil [17,22,24,37]. The total scan time for bi-component T2* and MT modeling was 45 min. However, more investigation is required to achieve fast, accurate, and clinically viable quantitative 3D UTE imaging techniques.

5. Conclusion

Two-pool MT modeling and bi-component T2* fitting techniques were investigated for their capability of cortical bone porosity assessment as measured through histomorphometric analyses performed on submicron resolution histology images. MMF from MT modeling as well as Frac1 and T2*1 from bi-component T2* fitting showed strong correlations with histomorphometric total and large-pores porosities as well as with μCT-based porosity. Remarkably, studied UTE-MRI techniques were able to detect small pores variations with moderate correlations. This study highlighted the capability of UTE-MRI techniques for detecting variation of bone porosity in the form of pores below the range detectable by μCT, including lacunae and small Haversian canals, which can contribute differently in bone disease, injury, and remodeling.

Conflict of interest statement

The authors have no conflicts of interest to declare.

Acknowledgements

The authors acknowledge grant support from NIH (1R21AR073496, R01AR068987, 1R01AR062581-01A1, T32EB005970) and VA Clinical Science and Rehabilitation R&D Awards (I01CX001388 and I01RX002604).

References

[1] E.Y. Chang, J. Du, C.B. Chung, UTE imaging in the musculoskeletal system, J. Magn. Reson. Imaging 41 (2015) 870–883, https://doi.org/10.1002/jmri.24713.

[2] J. Du, G.M. Bydder, Qualitative and quantitative ultrashort-TE MRI of cortical bone, NMR Biomed. 26 (2013) 489–506, https://doi.org/10.1002/nbm.2906.

[3] M. Granke, A.J. Makowski, S. Uppuganti, M.D. Does, J.S. Nyman, Identifying novel clinical surrogates to assess human bone fracture toughness, J. Bone Miner. Res. 30 (2015) 1290–1300, https://doi.org/10.1002/jbmr.2452.

[4] G.M. Treece, A.H. Gee, C. Tonkin, S.K. Ewing, P.M. Cawthon, D.M. Black, K.E.S. Poole, Predicting hip fracture type with cortical bone mapping (CBM) in the osteoporotic fractures in men (MrOS) study, J. Bone Miner. Res. 30 (2015) 2067–2077, https://doi.org/10.1002/jbmr.2552.

[5] A.C. Seifert, F.W. Wehrli, Solid-state quantitative 1H and 31P MRI of cortical bone in humans, Curr. Osteoporos. Rep. (2016) 1–10, https://doi.org/10.1007/s11914-016-0307-2.

[6] M. Granke, M.D. Does, J.S. Nyman, The role of water compartments in the material properties of cortical bone, Calcif. Tissue Int. 97 (2015) 292–307, https://doi.org/10.1007/s00223-015-9977-5.

[7] J.S. Nyman, Q. Ni, D.P. Nicolella, X. Wang, Measurements of mobile and bound water by nuclear magnetic resonance correlate with mechanical properties of bone,

Bone 42 (2008) 193–199, https://doi.org/10.1016/j.bone.2007.09.049.

[8] C.S. Rajapakse, M. Bashoor-Zadeh, C. Li, W. Sun, A.C. Wright, F.W. Wehrli, Volumetric cortical bone porosity assessment with MR imaging: validation and clinical feasibility, Radiology 276 (2015) 526–535, https://doi.org/10.1148/radiol.15141850.

[9] J. Du, J.C. Hermida, E. Diaz, J. Corbeil, R. Znamirowski, D.D. D'Lima, G.M. Bydder, Assessment of cortical bone with clinical and ultrashort echo time sequences, Magn. Reson. Med. 70 (2013) 697–704, https://doi.org/10.1002/mrm.24497.

[10] M.K. Manhard, S. Uppuganti, M. Granke, D.F. Gochberg, J.S. Nyman, M.D. Does, MRI-derived bound and pore water concentrations as predictors of fracture resistance, Bone 87 (2016) 1–10, https://doi.org/10.1016/j.bone.2016.03.007.

[11] E. Diaz, C.B. Chung, W.C. Bae, S. Statum, R. Znamirowski, G.M. Bydder, J. Du, Ultrashort echo time spectroscopic imaging (UTESI): an efficient method for quantifying bound and free water, NMR Biomed. 25 (2012) 161–168, https://doi.org/10.1002/nbm.1728.

[12] J. Du, M. Carl, M. Bydder, A. Takahashi, C.B. Chung, G.M. Bydder, Qualitative and quantitative ultrashort echo time (UTE) imaging of cortical bone, J. Magn. Reson. 207 (2010) 304–311, https://doi.org/10.1016/j.jmr.2010.09.013.

[13] J. Chen, E.Y. Chang, M. Carl, Y. Ma, H. Shao, B. Chen, Z. Wu, J. Du, Measurement of bound and pore water T1 relaxation times in cortical bone using three-dimensional ultrashort echo time cones sequences, Magn. Reson. Med. 77 (2016) 2136–2145, https://doi.org/10.1002/mrm.26292.

[14] J. Du, E. Diaz, M. Carl, W.C. Bae, C.B. Chung, G.M. Bydder, Ultrashort echo time imaging with bicomponent analysis, Magn. Reson. Med. 67 (2012) 645–649, https://doi.org/10.1002/mrm.23047.

[15] M.K. Manhard, J.S. Nyman, M.D. Does, Advances in imaging approaches to fracture risk evaluation, Transl. Res. 181 (2017) 1–14, https://doi.org/10.1016/j.trsl.2016.09.006.

[16] W.C. Bae, P.C. Chen, C.B. Chung, K. Masuda, D. D'Lima, J. Du, Quantitative ultrashort echo time (UTE) MRI of human cortical bone: correlation with porosity and biomechanical properties, J. Bone Miner. Res. 27 (2012) 848–857, https://doi.org/10.1002/jbmr.1535.

[17] X. Lu, S. Jerban, L. Wan, Y. Ma, H. Jang, N. Le, W. Yang, E.Y. Chang, J. Du, Three dimensional ultrashort Echo time imaging with tri-component analysis for human cortical bone, Magn. Reson. Med. (2019), https://doi.org/10.1002/mrm.27718.

[18] M.K. Manhard, R.A. Horch, K.D. Harkins, D.F. Gochberg, J.S. Nyman, M.D. Does, Validation of quantitative bound- and pore-water imaging in cortical bone, Magn. Reson. Med. 71 (2014) 2166–2171, https://doi.org/10.1002/mrm.24870.

[19] R. Biswas, W.C. Bae, E. Diaz, K. Masuda, C.B. Chung, G.M. Bydder, J. Du, Ultrashort echo time (UTE) imaging with bi-component analysis: bound and free water evaluation of bovine cortical bone subject to sequential drying, Bone 50 (2012) 749–755, https://doi.org/10.1016/j.bone.2011.11.029.

[20] Y. Ma, A. Tadros, J. Du, E.Y. Chang, Quantitative two-dimensional ultrashort echo time magnetization transfer (2D UTE-MT) imaging of cortical bone, Magn. Reson. Med. (2017), https://doi.org/10.1002/mrm.26846.

[21] Y. Ma, H. Shao, J. Du, E.Y. Chang, Ultrashort echo time magnetization transfer (UTE-MT) imaging and modeling: magic angle independent biomarkers of tissue properties, NMR Biomed. 29 (2016) 1546–1552, https://doi.org/10.1002/nbm.3609.

[22] S. Jerban, Y. Ma, L. Wan, A.C. Searleman, H. Jang, R.L. Sah, E.Y. Chang, J. Du, Collagen proton fraction from ultrashort echo time magnetization transfer (UTE-MT) MRI modelling correlates significantly with cortical bone porosity measured with micro-computed tomography (μCT), NMR Biomed. 32 (2019) 1–10, https://doi.org/10.1002/nbm.4045.

[23] E.Y. Chang, W.C. Bae, H. Shao, R. Biswas, S. Li, J. Chen, S. Patil, R. Healey, D.D.D. Lima, C.B. Chung, J. Du, Ultrashort echo time magnetization transfer (UTE-MT) imaging of cortical bone, NMR Biomed. 28 (2015) 873–880, https://doi.org/10.1002/nbm.3316.

[24] S. Jerban, Y. Ma, A. Nazaran, E.W. Dorthe, E. Cory, M. Carl, D. D'Lima, R.L. Sah, E.Y. Chang, J. Du, D. D'Lima, R.L. Sah, E.Y. Chang, J. Du, Detecting stress injury (fatigue fracture) in fibular cortical bone using quantitative ultrashort echo time-magnetization transfer (UTE-MT): an ex vivo study, NMR Biomed. 31 (2018) e3994, https://doi.org/10.1002/nbm.3994.

[25] S.C. Cowin, Bone poroelasticity, J. Biomech. 32 (1999) 217–238, https://doi.org/10.1016/S0021-9290(98)00161-4.

[26] X. Wang, Q. Ni, Determination of cortical bone porosity and pore size distribution using a low field pulsed NMR approach, J. Orthop. Res. 21 (2003) 312–319, https://doi.org/10.1016/S0736-0266(02)00157-2.

[27] S. Jerban, A. Sweedy, G. Baroud, M. Bohner, Fuzzy distance transform (FDT) versus distance transform (DT) applied to different range of pore sizes, 25th Interdiscip. Res. Conf. Inject. Osteoartic. Biomater. Bone Augment. Proced., Toronto, 2015 (p. poster No 25).

[28] S. Jerban, S. Elkoun, Individual pore and interconnection size analysis of macroporous ceramic scaffolds using high-resolution X-ray tomography, Mater. Charact. 118 (2016) 454–467, https://doi.org/10.1016/j.matchar.2016.06.030.

[29] Y. Ma, E.Y. Chang, M. Carl, J. Du, Quantitative magnetization transfer ultrashort echo time imaging using a time-efficient 3D multispoke cones sequence, Magn. Reson. Med. 00 (2017) 1–9, https://doi.org/10.1002/mrm.26716.

[30] P.T. Gurney, B.A. Hargreaves, D.G. Nishimura, Design and analysis of a practical 3D cones trajectory, Magn. Reson. Med. 55 (2006) 575–582, https://doi.org/10.1002/mrm.20796.

[31] M. Carl, G.M. Bydder, J. Du, UTE imaging with simultaneous water and fat signal suppression using a time-efficient multispoke inversion recovery pulse sequence, Magn. Reson. Med. 76 (2015) 577–582, https://doi.org/10.1002/mrm.25823.

[32] Y.-J. Ma, Y. Zhu, X. Lu, M. Carl, E.Y. Chang, J. Du, Short T_2 imaging using a 3D double adiabatic inversion recovery prepared ultrashort echo time cones (3D DIR-UTE-Cones) sequence, Magn. Reson. Med. 00 (2017) 1–9, https://doi.org/10.1002/mrm.26908.

[33] S. Li, E.Y. Chang, W.C. Bae, C.B. Chung, S. Gao, S. Bao, G.M. Bydder, Y. Hua, J. Du, Ultrashort echo time bi-component analysis of cortical bone - a field dependence study, Magn. Reson. Med. 71 (2014) 1075–1081, https://doi.org/10.1002/mrm.24769.

[34] T. Hildebrand, P. Rüegsegger, A new method for the model-independent assessment of thickness in three-dimensional images, J. Microsc. 185 (1997) 67–75, https://doi.org/10.1046/j.1365-2818.1997.1340694.x.

[35] S. Jerban, S. Elkoun, Novel linear intercept method for characterizing micropores and grains in calcium phosphate bone substitutes, Mater. Charact. 119 (2016) 216–224, https://doi.org/10.1016/j.matchar.2016.08.008.

[36] A. Darabi, F. Chandelier, G. Baroud, Morphometric analysis of trabecular bone thickness using different algorithms, Can. J. Electr. Comput. Eng. 32 (2007) 157–163, https://doi.org/10.1109/CJECE.2007.4413127.

[37] L. Wan, W. Zhao, Y. Ma, S. Jerban, A.C. Searleman, M. Carl, E.Y. Chang, G. Tang, J. Du, Fast quantitative three-dimensional ultrashort echo time (UTE) magnetic resonance imaging of cortical bone using extended cones sampling, Magn. Reson. Med. (2019), https://doi.org/10.1002/mrm.27715.